

# Linear array transducer for high-power airborne ultrasound using flextensional structure

Jun Yamamoto, Yosuke Mizuno, Marie Tabaru, and Kentaro Nakamura

Precision and Intelligence Laboratory, Tokyo Institute of Technology, Yokohama 226-8503, Japan

Received December 12, 2014; revised March 2, 2015; accepted April 6, 2015; published online June 29, 2015

To change the direction of ultrasonic irradiation without moving a transducer, a high-power airborne ultrasonic transducer for a one-dimensional phased array system was designed and tested. A flextensional element transducer with higher-mode bending vibration was fabricated to obtain a high vibration amplitude over a wide aperture, where a phase-compensating stepped structure was employed. The width of the main lobe at half maximum and the sidelobe level were measured to be 14.3 deg and 0.78, respectively. The maximal sound pressure of 132 dB (0 dB re. 0.02 mPa) was obtained under the applied voltage of 4.0 V. The beam steering characteristics of a phased array using eight elements were compared with the simple theory. © 2015 The Japan Society of Applied Physics

## 1. Introduction

There are many application fields of high-power airborne ultrasound, such as noncontact levitation,<sup>1–7)</sup> nondestructive testing,<sup>8–11)</sup> removal of solid or liquid particles,<sup>12–15)</sup> and defoaming.<sup>16,17)</sup> In such fields, the frequency range from 20 to 40 kHz is practically used, and the sound pressure level sometimes exceeds 160 dB. It is required that the direction of radiation be changed quickly through an electrical signal for precise control and increase in the efficiency of the target process. For levitation applications, for example, it is required that the position of small objects or droplets be shifted in a linear direction by changing the direction of ultrasonic irradiation.<sup>1,3,5)</sup> High-power airborne ultrasound is usually generated by using a flexural vibrating plate excited by a Langevin transducer with a horn, the directivity of which is fixed.<sup>16–21)</sup> To change the direction of ultrasonic irradiation linearly without moving the transducer, a one-dimensional phased array system should be used.

Several studies have already been reported on a phased array for high-power airborne ultrasound, where conventional commercial ultrasonic sensors were integrated.<sup>7,22–27)</sup> However, the sound pressure of a commercial transducer is limited.<sup>23)</sup> The diameter of a sensor, usually approximately 10 mm, is larger than the wavelength in air, 8.5 mm at a driving frequency of 40 kHz.<sup>28)</sup> Thus, it is difficult to have a smaller spacing between two adjacent transducers, and unwanted grating lobes are generated. A conventional airborne transducer is composed of a very thin aluminum horn and a bending piezoelectric disc. The resonance frequency is largely changed or the vibration displacement is easily lowered, even if a droplet, for example, is attached to the radiator horn. This structure is too fragile to be used for handling liquid or for a harsh environment.

The objective of this study is to develop a high-power ultrasonic transducer applicable for a one-dimensional phased array with a water-proof and dust-proof capability by eliminating any fragile structure. In this paper, we report the first prototype of the transducer, the fundamental characteristics of the element transducer, and the test of the beam steering operation for an eight-element array system, introducing flextensional and stepped structures.

## 2. Structure of the linear array transducer

Figure 1 shows the conceptual structure of a one-dimensional phased array system, which is composed of linearly arrayed

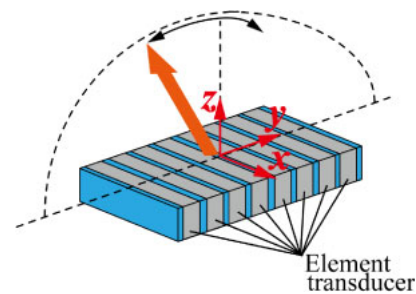


Fig. 1. (Color online) Conceptual configuration of one-dimensional array and the coordinate system.

element transducers. The radiation surface of each element has a long narrow rectangular shape.<sup>28)</sup> In this figure, the  $x$ -axis is the longer direction of the radiation surface, the  $y$ -axis the arrayed direction, and the  $z$ -axis the radiation direction. Beam steering is performed in the  $yz$ -plane through phased-drive, and a small beam width is obtained in the  $xz$ -plane owing to the large beam width in the  $x$ -direction. The  $x$ -length of the radiation surface should be four or five times the wavelength in air for the small beam width,<sup>29)</sup> while the  $y$ -width of the radiation surface should be less than the wavelength to inhibit the generation of grating lobes.<sup>28)</sup> In this study, the working frequency is set at 30 kHz for the trial. The thickness of the radiation surface for one element should be less than the wavelength to inhibit the generation of grating lobes in phased-array operation. The width of the radiation surface is designed to be larger than five times the wavelength to induce irradiation at angles confined within 20–30 deg. Thus, the radiation surface was determined to be  $70 \times 5 \text{ mm}^2$  in the prototyping. The thin rectangular radiation surface is required to vibrate uniformly at a high vibration amplitude to radiate the main beam in the  $z$ -direction. However, it is generally difficult to have a uniform vibration over a large surface. On the other hand, higher-mode bending vibrations in a flextensional structure can be easily generated on a bar at a high vibration amplitude,<sup>30)</sup> such vibrations have an out-of-phase amplitude and result in a split radiation pattern. Thus, the stepped surface to compensate the phase inverse was introduced; this method has already been used in conventional flexural vibrating plates.<sup>18–22)</sup> The detailed structure based on this concept has been explored as follows.

The four structures shown in Fig. 2 were investigated through finite element analysis (FEA). Figure 2(a) shows the

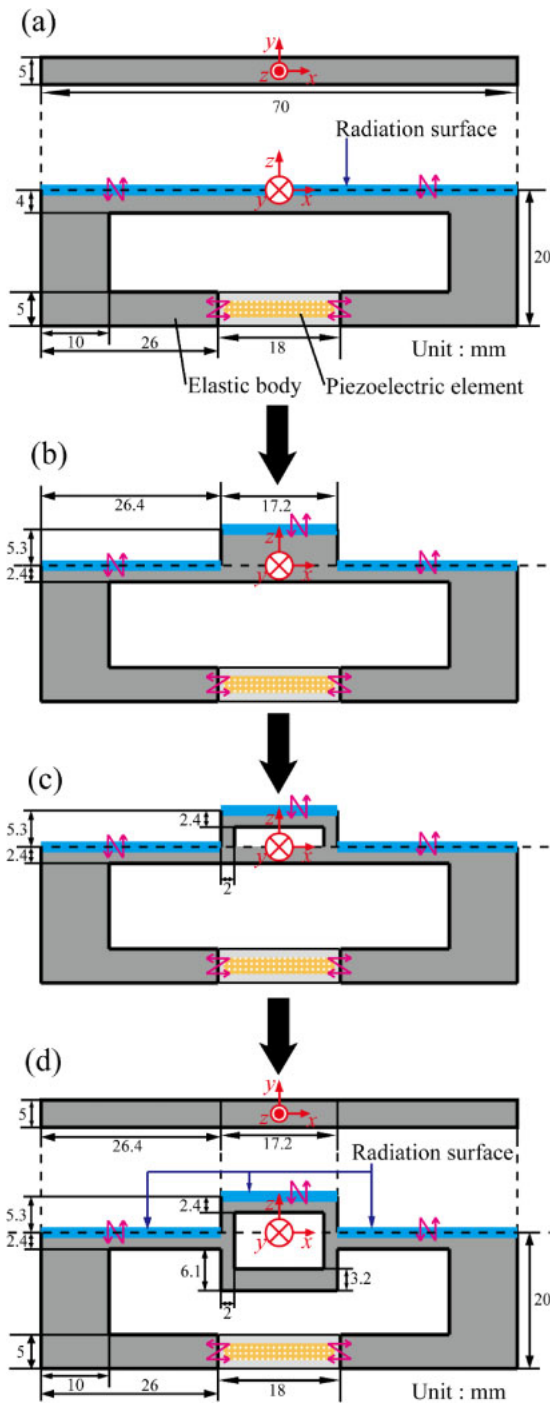


Fig. 2. (Color online) Structures of element transducers.

fundamental configuration including a flextensional structure, where a multilayered piezoelectric ceramics element of  $5 \times 5 \times 18 \text{ mm}^3$  (PI P885T0001) is inserted in a duralumin (A7075P) frame. The duralumin frame and piezoelectric element are bonded to each other with epoxy. The upper surface indicated by a blue line in Fig. 2 is the radiating surface. Figure 3(a) shows the calculated vibration mode, whose eigenfrequency is 33.3 kHz. A one-and-a-half-wavelength bending vibration is generated on the radiation surface, and the vibration in the central part is out of phase to the rest of the radiation surface. The calculated curve in Fig. 4(a) shows the far field directivities calculated from the vibration velocity distribution  $u(x, y)$  obtained in Fig. 3(a) using

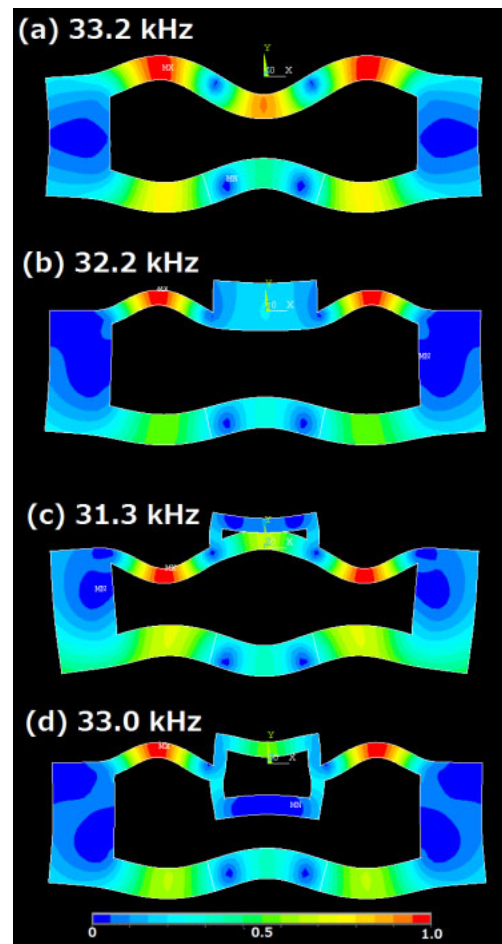


Fig. 3. (Color online) Vibration modes for each transducer model calculated using FEA. The color indicates the magnitude of the vibration displacement normalized by the maximum value.

$$P(R, \theta) = j\rho f \iint_S u(x, y) \frac{\exp(-jkr)}{r} dS, \quad (1)$$

$$r = \sqrt{(x - R \sin \theta)^2 + y^2 + (R \cos \theta)^2},$$

where  $P(R, \theta)$  is the sound pressure at the distance of  $R$  ( $= 1.0 \text{ m}$ ) and the angle  $\theta$ ,  $j$  is the imaginary unit,  $\rho$  is the density of air ( $= 1.225 \text{ kg/m}^3$ ),  $f$  is the frequency,  $k$  is the wave number, and  $c$  is the sound speed ( $= 340 \text{ m/s}$ ).<sup>31)</sup> The integral is carried out over the radiation surface  $S$ . The result is normalized with the maximum value. The highest radiation appears in the angled directions as shown in Fig. 4(a). This is due to the vibration distribution with both positive and negative displacements on the surface as mentioned previously. The fundamental bending mode, which has an in-phase displacement all over the surface, can be excited at only a lower frequency. If the thickness of the bending part is increased, the resonance frequency will increase, but the excited vibration amplitude will decrease.

Thus, the steps of 5.3 mm in the central part of the radiation surface were introduced as shown in Fig. 2(b). The step size is adjusted to half the wavelength in air to cancel the negative phase in the vibration as illustrated in Fig. 5, and then a uniform wave front is obtained in air. Figure 3(b) shows the vibration modes calculated by FEA. This method was originally employed in the previous study using a plate and a Langevin transducer.<sup>17)</sup> The thickness of the side of the

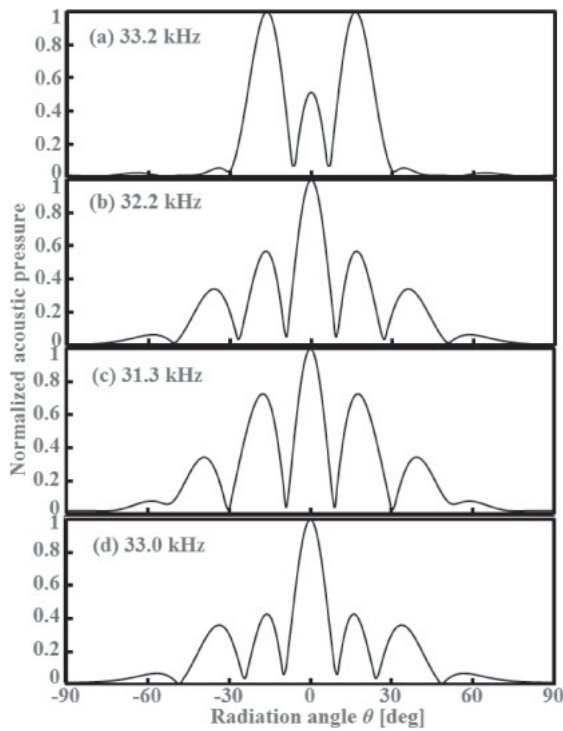


Fig. 4. Directivity patterns calculated using the vibration distribution given in Fig. 3.

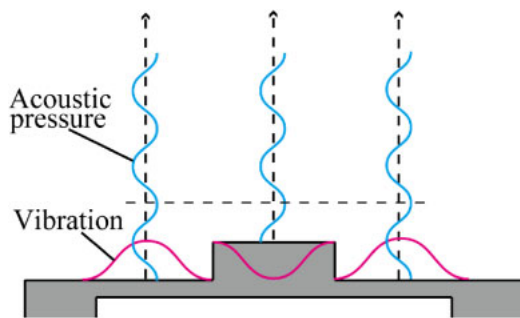


Fig. 5. (Color online) Phase compensation mechanism using the stepped structure.

radiation surface is reduced to 2.4 mm to increase the vibration with smaller mass and to keep the resonance frequency at approximately 30 kHz. The vibration in the central part of the radiation surface is much smaller than that on the side because of its weight, and the sidelobe level is higher than half the main lobe level, as shown in Fig. 4(b).

Next, to increase the vibration amplitude in the central part of the radiation surface, a hole is created in the stepped part, as shown in Fig. 2(c). Against our expectations, the central part has a smaller vibration that is in phase with the other parts, as shown in Fig. 3(c). The sidelobe level increases, as shown in Fig. 4(c). This distribution pattern was not sufficiently changed by alternating the thickness of the radiation part.

To generate the vibration in the central part, the steps are installed on the bottom side, as well as on the top, with the hole introduced, as shown in Fig. 2(d). The rectangular hole in the stepped part is enlarged to resonate in the expansion mode, as demonstrated in Fig. 3(d). Figure 6 illustrates essential parameters of the radiation part:  $s$  is the height of the

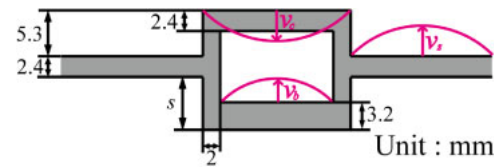


Fig. 6. (Color online) Measurements of the radiation parts.

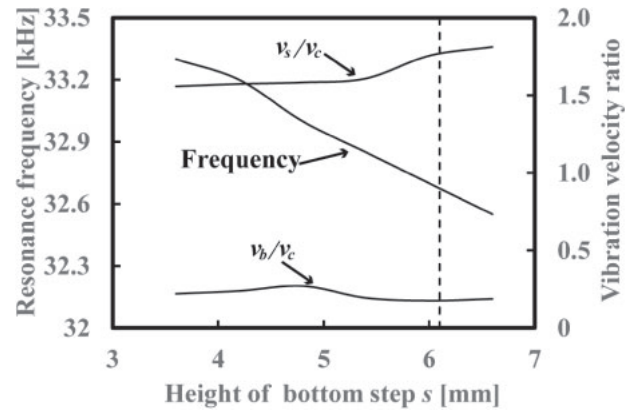


Fig. 7. Resonance frequency and vibration velocity ratio vs  $s$ .

bottom step,  $v_c$  is the maximum vibration velocity in the central part of the radiation surface,  $v_s$  is the velocity on the side, and  $v_b$  the velocity at the bottom. The ratio  $v_s/v_c$  should be less than 1.0 to decrease the sidelobe level of the directivity in the  $xz$ -plane, while the ratio  $v_b/v_c$  should be as low as possible to prevent the bottom step from affecting the directivity. Figure 7 shows the resonance frequency and the vibration velocity ratios  $v_s/v_c$  and  $v_b/v_c$  as functions of  $s$ . The ratio  $v_s/v_c$  is always higher than 1.0 for the given range of  $s$ , although the ratio  $v_b/v_c$  becomes minimum at  $s = 6.1$  mm. In this prototype, although the ratio  $v_s/v_c$  did not meet the requirement,  $s = 6.1$  was employed for the element transducer, because the resonance frequency becomes closer to 30.0 kHz and the ratio  $v_b/v_c$  is minimum. The sidelobe level is expected to be less than half the main lobe level, as shown in Fig. 4(d).

### 3. Characteristics of the element transducer

#### 3.1 Vibration velocity distribution

The vibration velocity distribution along the  $x$ -axis on the radiation surface of the model in Fig. 2(d) was measured with a laser Doppler velocimeter (LDV) at a frequency of 30.0 kHz when a peak-to-peak voltage of 1.0 V was applied to the piezoelectric element. Figure 8 shows the results, where the vertical dotted lines indicate the positions of the steps.

#### 3.2 Directional characteristics of the radiated field

The directivities in the  $xz$ -plane and  $yz$ -plane were measured 1.0 m away from the radiation surface with a 1/8-in. condenser microphone (ACO 7118). In the experiment, the microphone was fixed and the element under test was rotated around the axis of the coordinate system presented in Fig. 2(d). The side of the transducer was surrounded by a urethane sponge to minimize the radiation from unwanted parts. The results are shown in Fig. 9 with red dots and

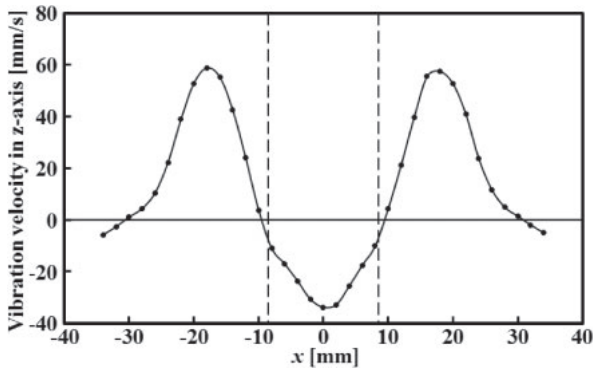


Fig. 8. Vibration velocity distribution measured at 30 kHz.

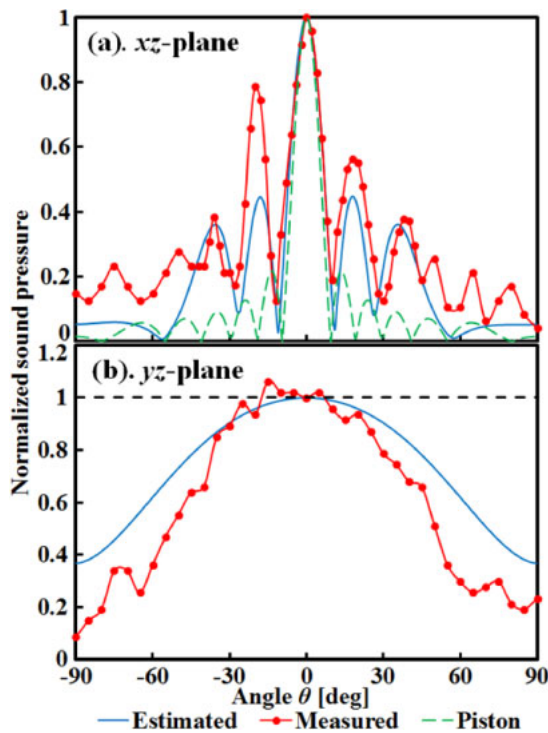


Fig. 9. (Color online) Directivity patterns at 30 kHz.

curves. The blue curve is the sound pressure  $P(R, \theta)$  calculated from Eq. (1), where the measured vibration distribution of Fig. 8 was used for  $u(x, y)$ . The measured and estimated values were normalized with each maximum. In the  $xz$ -plane, the green dotted line represents the directivity of the piston vibrator with the same aperture calculated from<sup>29)</sup>

$$D(\theta) = \frac{\sin(ka \sin \theta)}{ka \sin \theta}, \quad (2)$$

where  $a$  is half the larger width of the radiation surface.<sup>28)</sup> Table I shows the full width at half maximum (FWHM) and the sidelobe level (SL) of each directivity in Fig. 9(a). The measured FWHM is almost the same as the estimated and piston value, while the sidelobe level is higher than the calculations. It is thought that this discrepancy is caused by the radiation leaked from other vibrating surfaces such as the side of the step and other surfaces. In the directivity measured in the  $yz$ -plane, the measured value is almost in agreement with the estimated value, as shown in Fig. 9(b).

Table I. Comparison of the directivity characteristics at 30.0 kHz (FWHM, full width at half maximum; SL, sidelobe level).

	FWHM (deg)	SL
Measured	14.3	0.78
Estimated	14.0	0.44
Piston	11.4	0.22

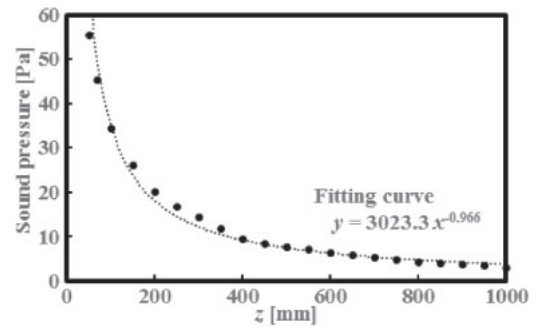


Fig. 10. Sound pressure in free field as a function of the distance.

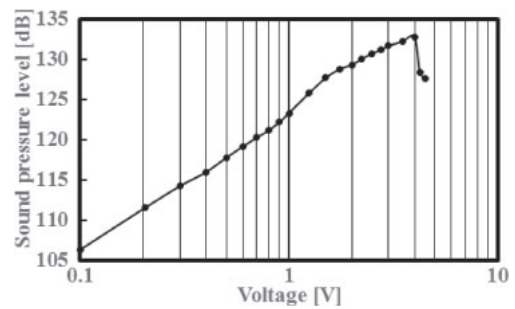


Fig. 11. Sound pressure level as a function of the voltage.

### 3.3 Measurement at high vibration amplitude

Figure 10 shows the distance characteristics of the prototype transducer measured along the  $z$ -axis as well as a fitted curve. It was confirmed that the sound pressure of the prototype transducer is almost inversely proportional to the distance in this range. The measurement of sound pressure at a high vibration amplitude was performed at a distance of 300 mm. To prevent the piezoelectric element from breaking down due to thermal stress, a burst signal was employed as the input. Figure 11 shows the results. The output sound pressure level increased proportionally to the input voltage up to 132 dB (0 dB = 0.02 mPa). When the input voltage exceeded 4.0 V, the sound pressure level dropped. This sudden decrease was caused by the weakening of the bonding part between the duralumin frame and the piezoelectric element, and the sound pressure level never recovered to the original value.

## 4. Eight-element phased array characteristics

### 4.1 Experimental setup

Figure 12 shows a photograph of the eight-element linear array using the prototype transducers. The width of the element transducer is 5 mm and the spacing between the elements is 2 mm, and then the interval between the elements is 7 mm, which is smaller than the wavelength at 30 kHz. The total aperture of the array is  $70 \times 54 \text{ mm}^2$ . The elements are

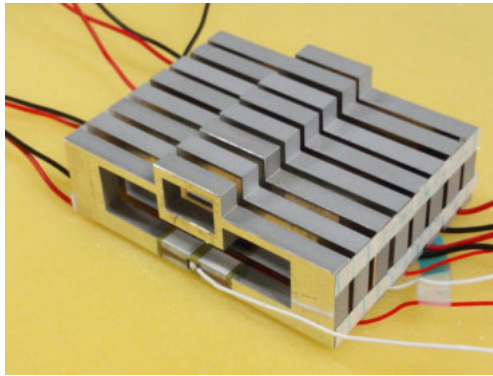


Fig. 12. (Color online) Photograph of the eight-element array.

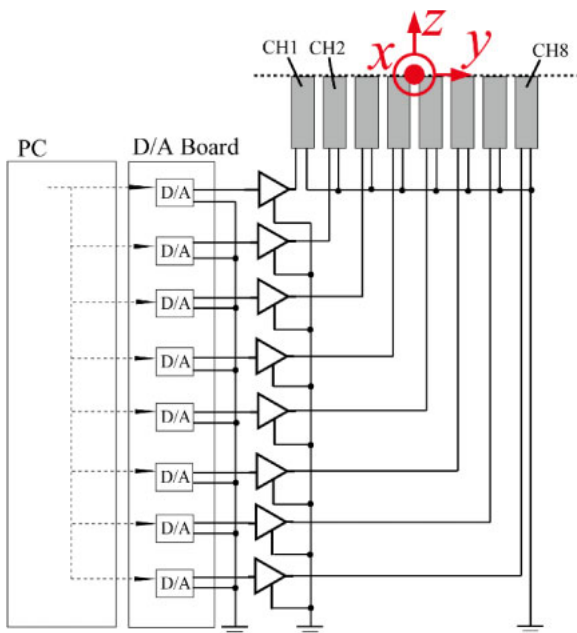


Fig. 13. (Color online) Driving electronics.

fixed together using tapes at the positions exhibiting small vibration displacements found in Fig. 3(d).

Figure 13 illustrates driving electronics for the array. A digital-to-analog (D/A) converter board (National Instruments PCI-7831R) is controlled by a PC generated eight-phase sinusoidal signals, which are fed to the element transducers via linear power amplifiers (National Semiconductor LM380N). Each element (CH1–CH8) has a slightly different resonance frequency owing to uncertainty in fabrication, and thus velocities and phases deviate between the transducers for the same driving frequency. The resonance characteristics of each transducer are summarized in Table II. The driving frequency is set at 30.3 kHz, which is slightly higher than all the resonance frequencies. The amplitudes and phases of the driving voltages were so compensated that the amplitudes and phases of the vibration velocities would be the same. Table III shows the resultant amplitudes and phases of the vibration velocities measured using the LDV. Phase differences could not be completely corrected, because the minimum pitch in the phase difference controlled by the D/A converter used in the experiment was 14.7 deg at this frequency.

Table II. Resonance characteristics of the eight element transducers.

	Resonance frequency (kHz)	Admittance (mS)	Quality factor
CH1	30.29	329	79
CH2	30.13	476	133
CH3	30.20	321	97
CH4	29.75	458	159
CH5	30.09	465	154
CH6	30.25	576	133
CH7	29.78	606	94
CH8	30.01	368	160

Table III. Errors in the vibration velocity amplitude and the phase of each element.

	Vibration velocity (m/s)	Phase (deg)
CH1	0.116	0
CH2	0.140	-4
CH3	0.101	-2
CH4	0.110	+2
CH5	0.122	-7
CH6	0.116	-5
CH7	0.104	-3
CH8	0.091	-5

#### 4.2 Beam steering characteristics

The directivities in the  $yz$ -plane were measured 1.0 m away from the array at the phase differences of  $-66$ ,  $-36.6$ ,  $0$ ,  $29.4$ , and  $58.8$  deg. In the experiment, the microphone was fixed and the array was rotated around the axis set at the center of the radiation surface, as presented in Fig. 13. Figure 14 shows the directivity pattern for each phase difference. The red dots and curves indicate the measured sound pressure. The blue solid and black dotted curves indicate the values calculated using Eq. (1) with and without the variations in the amplitude and phase shown in Table III, respectively. The directivity is normalized at each peak sound pressure. Figure 14 shows the angles of the main lobe for the phase differences  $\Delta\varphi$  given between the transducers. The ideal value in Fig. 15 is calculated from<sup>28)</sup>

$$\theta = \frac{180}{\pi} \sin^{-1} \left( \frac{\Delta\varphi}{360} \frac{c}{d \cdot f} \right), \quad (3)$$

where  $\theta$  is the radiation angle and the interval of the source  $d$  is 7 mm. It was confirmed that the radiation angle was successfully controlled by changing the phase difference. The maximum values of the sound pressure level were 118 dB for the phase  $-66.0$  deg, 121 dB for  $-36.6$  deg, 123 dB for 0 deg, 122 dB for 29.4 deg, and 120 dB for 58.8 deg. The maximum output sound pressure for the eight-element phased array is expected to be 150 dB, if it is simply calculated by multiplying the sound pressure of a single element eight times. It was difficult to obtain such a high output, because the resonance frequencies of the elements were not identical in the prototype transducers.

#### 5. Conclusions

The trial manufacture of a high-power airborne ultrasonic transducer for a one-dimensional phased array was per-

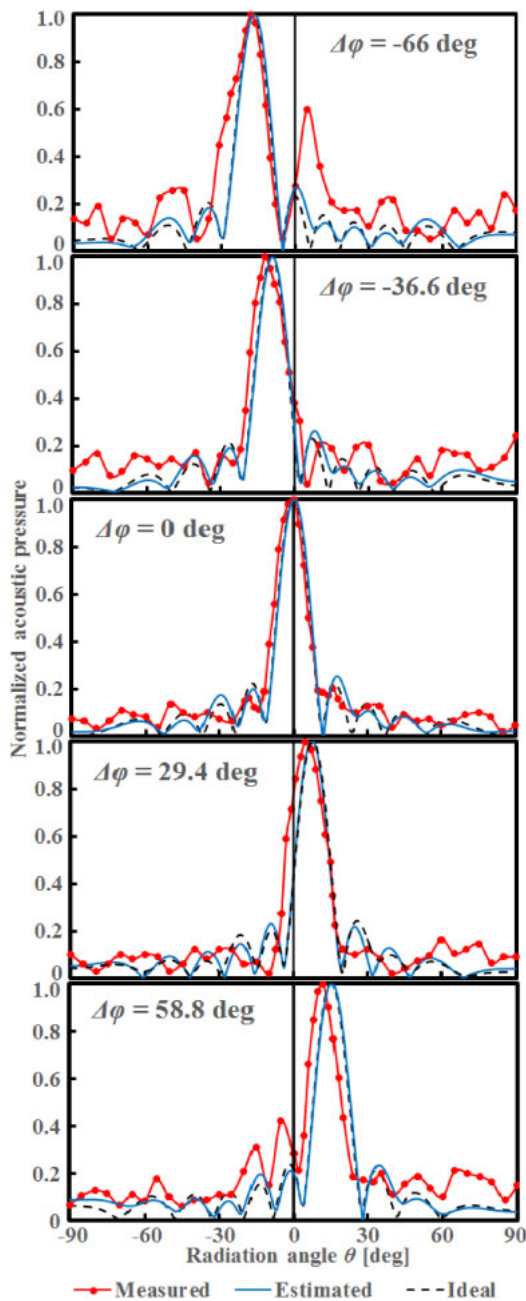


Fig. 14. (Color online) Directivity of the phased array.

formed. A radiation surface with steps was designed to have a uniform wave front in air, and the structure was modified to have a higher vibration amplitude. The directivity at 30.0 kHz showed the FWHM of 14.3 deg and the sidelobe level of 0.78. The sound pressure of 132 dB was obtained at the distance of 300 mm. It is necessary to optimize the shape of the transducer to obtain a higher vibration amplitude at the center of the radiation surface than in the side parts. Multilayered piezoelectric elements should be replaced by other low-loss elements for higher-amplitude operation.

The phased array characteristics obtained using eight transducers were tested. It was confirmed that, by changing

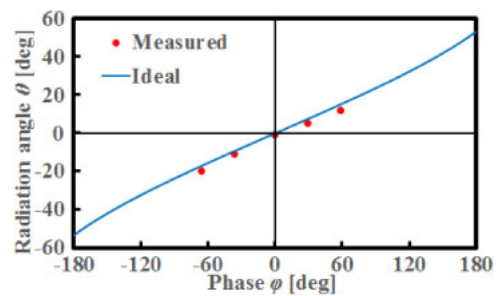


Fig. 15. (Color online) Beam steering characteristics.

the phase difference, the radiation angle can be controlled as we expected. The fabrication process is required to be improved to minimize the resonance frequency variation.

- 1) D. Koyama and K. Nakamura, *IEEE Trans. Ultrason. Ferroelectr. Freq. Control* **57**, 1152 (2010).
- 2) D. Koyama and K. Nakamura, *IEEE Trans. Ultrason. Ferroelectr. Freq. Control* **57**, 1434 (2010).
- 3) Y. Ito, D. Koyama, and K. Nakamura, *Acoust. Sci. Technol.* **31**, 420 (2010).
- 4) R. Kashima, S. Murakami, D. Koyama, K. Nakamura, and M. Matsukawa, *IEEE Trans. Ultrason. Ferroelectr. Freq. Control* **61**, 1024 (2014).
- 5) M. Ding, D. Koyama, and K. Nakamura, *Appl. Phys. Express* **5**, 097301 (2012).
- 6) R. Nakamura, Y. Mizuno, and K. Nakamura, *Jpn. J. Appl. Phys.* **52**, 07HE02 (2013).
- 7) T. Hoshi, Y. Ochiai, and J. Rekimoto, *Jpn. J. Appl. Phys.* **53**, 07KE07 (2014).
- 8) A. Osumi and Y. Ito, *J. Acoust. Soc. Am.* **133**, 3499 (2013).
- 9) A. Osumi and Y. Ito, *Proc. IEEE Int. Ultrasonics Symp.*, 2010, p. 2376.
- 10) A. Osumi, K. Doi, and Y. Ito, *Jpn. J. Appl. Phys.* **50**, 07HE30 (2011).
- 11) A. Osumi, M. Enomoto, and Y. Ito, *Jpn. J. Appl. Phys.* **53**, 07KC16 (2014).
- 12) G. J. Brereton and B. A. Bruno, *J. Sound Vib.* **173**, 683 (1994).
- 13) Y. Ito and M. Kotani, *Jpn. J. Appl. Phys.* **43**, 2840 (2004).
- 14) Y. Ito, S. Nakayama, and R. Miwa, *Jpn. J. Appl. Phys.* **38**, 3312 (1999).
- 15) Y. Ito, R. Kato, and A. Osumi, *Jpn. J. Appl. Phys.* **52**, 07HE12 (2013).
- 16) J. A. Gallego-Juarez, *Proc. IEEE Int. Ultrasonics Symp.*, 1994, p. 1343.
- 17) J. A. Gallego-Juárez, G. Rodríguez, V. Acosta, and E. Riera, *Ultrason. Sonochem.* **17**, 953 (2010).
- 18) A. Barone and J. A. Gallego Juarez, *J. Acoust. Soc. Am.* **51**, 953 (1972).
- 19) J. A. Gallego Juárez, *J. Sound Vib.* **26**, 411 (1973).
- 20) J. A. Gallego-Juarez, G. Rodríguez-Corral, and L. Gaete-Garretón, *Ultrasonics* **16**, 267 (1978).
- 21) H. Okada, M. Kurosawa, S. Ueha, and M. Masuda, *Jpn. J. Appl. Phys.* **33**, 3040 (1994).
- 22) T. Hoshi, T. Iwamoto, and H. Shinoda, *3rd Joint Eurohaptics Conf. Symp. Haptic Interfaces for Virtual Environment and Teleoperator Systems*, 2009, p. 256.
- 23) T. Hoshi, D. Abe, and H. Shinoda, *IEEE 18th Int. Symp. Robot and Human Interactive Communication*, 2009, p. 7.
- 24) T. Hoshi, M. Takahashi, and T. Iwamoto, *IEEE Trans. Haptics* **3**, 155 (2010).
- 25) T. Hoshi, *IEEE World Haptics Conf.*, 2011, p. 569.
- 26) T. Hoshi, *IEEE Haptics Sym.*, 2012, p. 399.
- 27) S. Takeoka and Y. Yamasaki, *Int. Congr. Acoustics*, 2010.
- 28) S. C. Wooh and Y. Shi, *Wave Motion* **29**, 245 (1999).
- 29) C. T. Molloy, *J. Acoust. Soc. Am.* **20**, 387 (1948).
- 30) T. Inoue, T. Nada, T. Miyama, K. Sugiuchi, and S. Takahashi, *Proc. IEEE Ultrasonics Symp.*, 1987, p. 765.
- 31) K. B. Ocheltree and L. A. Frizzell, *IEEE Trans. Ultrason. Ferroelectr. Freq. Control* **36**, 242 (1989).